Isolated attosecond pulse generation using multicycle pulses directly from a laser amplifier

Steve Gilbertson, Yi Wu, Sabih D. Khan, Michael Chini, Kun Zhao, Ximao Feng, and Zenghu Chang*
J. R. Macdonald Laboratory, Department of Physics, Kansas State University, Manhattan, Kansas 66506, USA
(Received 5 January 2010; published 13 April 2010)

Using a generalized version of double optical gating, we produced single isolated attosecond pulses with 2-mJ, 25-fs driving lasers. Temporal characterization revealed that the 160-as pulses are accompanied with very weak pre- and postpulses. The dependence of the extreme-ultraviolet spectrum on the carrier-envelope phase of the 25-fs laser exhibited a unique 2π periodicity, indicating the robustness of the subcycle gating.

DOI: 10.1103/PhysRevA.81.043810 PACS number(s): 42.65.Re, 42.65.Ky, 32.80.Qk

I. INTRODUCTION

Isolated attosecond pulses are important for current trends in cutting-edge physics concerning electron dynamics in atoms, molecules, and solids [1]. The field of attosecond science has greatly benefited in recent years from the various gating techniques developed for generating isolated attosecond pulses [2–9]. However, the previously demonstrated gating methods required starting with few-cycle femtosecond laser pulses with precisely controlled carrier-envelope (CE) phases. In order to produce 130-as pulses with the method of polarization gating, [10] input pulses with duration of 5 fs were required while the 80-as pulses produced with the amplitude gating method [11] required 3.3-fs pulses. Handling the broad spectra of the few-cycle driving lasers is difficult because high-order phase errors need to be corrected, which is the reason that it is a challenge to reproduce the driving laser pulses on a daily basis. So far, only a few labs in the world can produce and work with CE-phase-stabilized high-power sub-4-fs laser pulses.

The double optical gating (DOG) technique that was developed a few years ago [12,13] reduced this requirement. The technique is a combination of polarization gating and a weak second-harmonic pulse, also known as two-color gating [14]. This allowed multicycle lasers of up to 12 fs to be used for attosecond pulse generation while reducing losses in the conversion efficiency of extreme-ultraviolet (XUV) photons [15]. While these pulses are substantially easier to generate and work with experimentally, they still require a hollow-core fiber and chirped mirror set after the chirped pulse amplifier for spectral broadening and temporal compression. This limits the laser energy to a few mJ. Consequently, the flux of the isolated attosecond pulses is low ($\sim$100 pJ to 1 nJ). For nonlinear attosecond physics and attosecond pump-attosecond probe experiments, the flux should approach the μJ level.

Ideally, isolated attosecond pulses should be generated directly from Ti:sapphire chirped pulse amplifiers producing $\sim$25-fs pulses. Such laser systems are commercially available and many labs already have them. Not only does this aid in the ease with which the attosecond pulses can be generated, it also allows the flux of XUV photons to be scaled to higher levels by increasing the input pulse power. Since pettawatt class 30-fs lasers are available [16], this method can be utilized for the production of attosecond pulses with unprecedented pulse energy.

Generating attosecond pulses from an amplifier directly is very challenging since the gating needs to isolate a single attosecond pulse from a long attosecond pulse train. The main concern is the elimination of the contribution from the satellite pulses to produce isolated attosecond pulses with high contrast. Of the currently successful gating techniques, amplitude gating was not possible since its principle relied on very short input pulses. Also, both polarization gating and DOG with their ellipticity-dependent pulses created from a superposition of right and left circularly polarized pulses would give too low an XUV photon flux for 25-fs input pulse durations. This is because the upper-limit pulse duration is determined by depletion of the target from the leading edge of the ellipticity-dependent pulse [9,17].

Using a superposition of right and left elliptically polarized pulses in the DOG scheme was found to reduce the leading-edge ionization further than circularly polarized pulses. This led to a generalized method of DOG known as GDOG [18]. This technique was shown to be capable of generating 148-as pulses from a 28-fs amplifier with no hollow-core fiber pulse compression. The purpose of this article is to provide the details of the driving laser system and the generation scheme which were omitted due to space limitations of the letter (Ref. [18]), including the effects of the CE phase of the laser. Also, we wanted to show that the XUV flux generated and the pre- and postpulse contributions are comparable with that seen with other gating schemes. Finally, we examined the effects of the statistical noise on the temporal characterization of attosecond pulses using the frequency-resolved optical gating for the complete reconstruction of attosecond bursts (FROG-CRAB) [19] method. This determines the lower limit on how much integration time is required to generate data useful for accurately reconstructing the attosecond pulse generated with 25-fs lasers.

II. GATE WIDTH ANALYSIS

The ellipticity-dependent pulse with the fundamental frequency of the laser for the generalized DOG can be decomposed into two orthogonally polarized components known as the driving field and the gating field. The gating field is zero at the center of the pulse while the driving field is nonzero. This results in a one-cycle linearly polarized laser field, defined as the gate width for the attosecond pulse generation, while elsewhere in the pulse, the superposition of the driving and

*chang@phys.ksu.edu

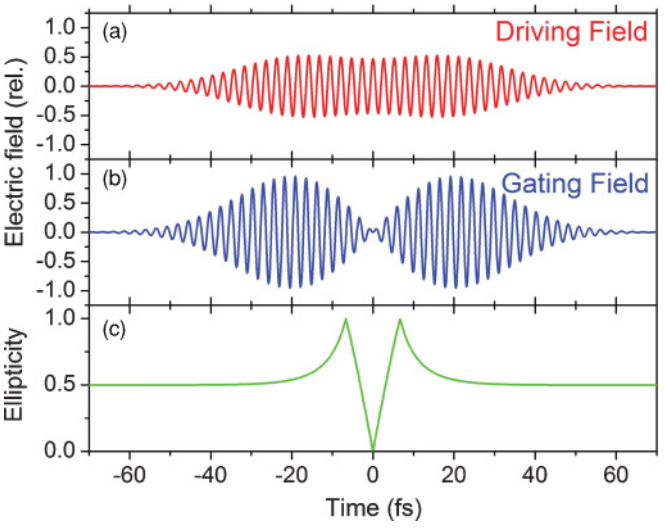

FIG. 1. (Color online) (a) The driving field of the ellipticity-dependent pulse generated with GDOG. The pulse duration is 25 fs and the delay, T_d, is 37 fs. (b) The corresponding gating field for the parameters in (a). (c) The time-dependent ellipticity calculated from the field components in (a) and (b).

gating fields gives some degree of elliptical polarization. The field components can be expressed as

$$E_{\text{drive}}(t) = E_0\varepsilon\{e^{-2\ln(2)[(t-T_d/2)/\tau_p]^2} + e^{-2\ln(2)[(t+T_d/2)\tau_p]^2}\} \times \cos(\omega_0 t + \varphi_{\text{CE}}), \quad (1)$$

$$E_{\text{gate}}(t) = E_0\{e^{-2\ln(2)[(t-T_d/2)/\tau_p]^2} - e^{-2\ln(2)[(t+T_d/2)/\tau_p]^2}\} \times \sin(\omega_0 t + \varphi_{\text{CE}}), \quad (2)$$

where ε is the ellipticity of the right and left circularly polarized pulses generated by the GDOG optics, τ_p is the laser pulse duration, φ_{CE} is the CE phase, ω_0 is the carrier frequency, and T_d is the delay between the left and right elliptically polarized pulses, which equals an integer number of the laser cycle. Figure 1(a) shows the driving field for a 25-fs, 780-nm laser pulse with $\varepsilon = 0.5$ while Fig. 1(b) shows the corresponding gating field.

These components can be used to find the time-dependent ellipticity of the pulse by taking the ratio of the envelopes of the gating field to the driving field, yielding

$$\xi(t) = \min\left[\frac{\left|1 - e^{-4\ln(2)(T_d/\tau_p^2)t}\right|}{\varepsilon\left[1 + e^{-4\ln(2)(T_d/\tau_p^2)t}\right]}, \frac{\varepsilon\left[1 + e^{-4\ln(2)(T_d/\tau_p^2)t}\right]}{\left|1 - e^{-4\ln(2)(T_d/\tau_p^2)t}\right|}\right]. \quad (3)$$

The time-dependent ellipticity is shown in Fig. 1(c). Since we are interested in the time range where the field is approximately linear, a Taylor expansion of Eq. (3) about the center of the pulse, or $t = 0$, keeping the first nontrivial term, yields

$$\xi(t) = \left|2\ln(2)\frac{T_d}{\varepsilon\tau_p^2}t\right|. \quad (4)$$

Solving Eq. (4) for t and multiplying by 2 gives the gate width equation,

$$\delta t_G \approx \varepsilon\frac{\xi_{\text{th}}}{\ln(2)}\frac{\tau_p^2}{T_d}, \quad (5)$$

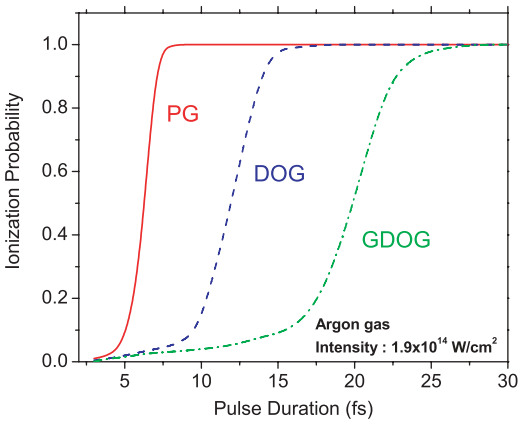

FIG. 2. (Color online) Ionization probability as a function of input laser pulse duration for polarization gating (PG, solid line), double optical gating (DOG, dashed line), and generalized double optical gating (GDOG, dot-dashed line). The peak intensity at the center of the gate was held constant at 1.9×10^{14} W/cm^2 for all cases. The gate width was half an optical cycle for PG and one full cycle for both DOG and GDOG.

where $\xi_{\text{th}} \approx 0.1$ is the threshold ellipticity for harmonic generation. As an example, for a 25-fs laser pulse with center wavelength of 780 nm and with $\varepsilon = 0.5$, T_d should be ~37 fs to ensure the gate width is one optical cycle, which is the spacing between the adjacent attosecond pulses in the train. Without the symmetry-breaking contribution of the second harmonic, the attosecond pulse spacing would be half of an optical cycle and T_d would need to be ~70 fs to effectively gate a single pulse in the train. This would lead to complete depletion of the target by the leading edge of the pulse.

The leading edge of the GDOG pulse with its strong ellipticity will obviously deplete the ground-state population of the gas target without contributing to the XUV photon flux. It was shown that this depletion strongly depends on the delay between the right and the left circularly polarized pulses in the case of DOG [12] and is reduced with DOG as compared to polarization gating. The depletion is further reduced in the GDOG case, implying that even longer pulse durations can be used without full depletion of the target. Figure 2 shows a calculation from the Ammosov, Delone, and Krainov (ADK) theory for the ionization of argon atoms from an oscillating laser field [20]. The calculation was done assuming the peak intensity at the center of the gate width was 1.9×10^{14} W/cm^2. From the cutoff law for harmonic generation [21], this gives a spectrum extending to ~50 eV which was the maximum experimentally obtained cutoff. From the figure, the depletion of GDOG pulses is greatly reduced even for pulses nearly 25 fs in duration as compared with that seen with polarization gating and even DOG. There are many other factors that contribute to the XUV photon flux, however, so this is a semiquantitative model. Also, it should be noted that in all cases shorter pulse durations will yield less depletion and higher photon fluxes are expected.

III. OPTICS FOR CREATING GDOG LASER FIELD

The optics consisted of a pair of birefringent quartz plates, a fused silica window, and a type-1 barium borate (BBO) crystal.

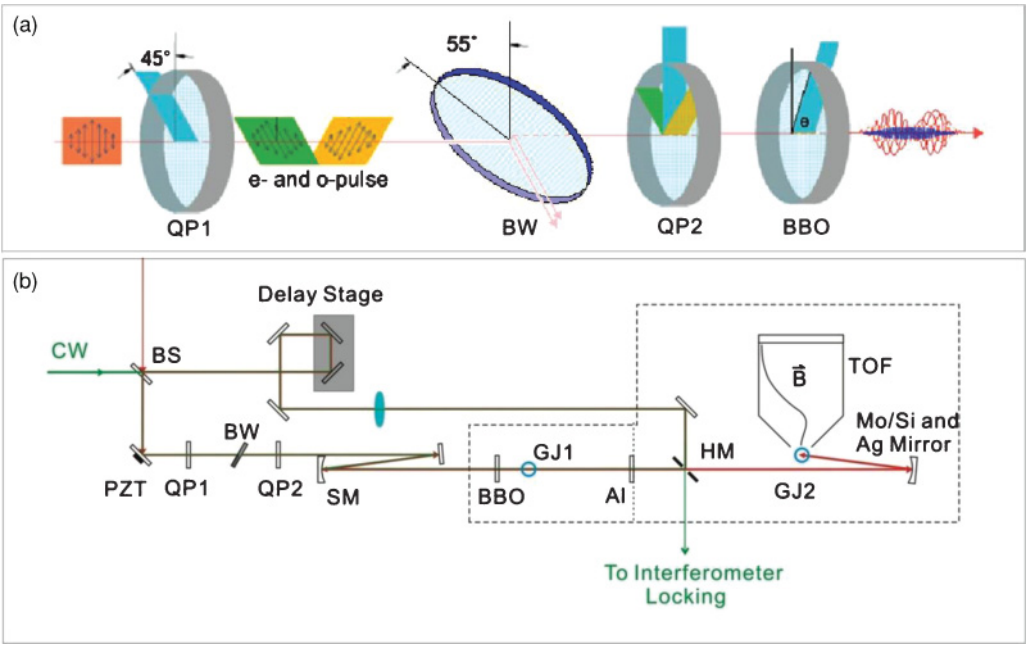

FIG. 3. (Color online) (a) The streak-camera setup; (b) the GDOG optics. BS, beam splitter; PZT, piezoelectric transducer; QP1 and QP2, quartz plates; BW, Brewster window; SM, spherical mirror; GJ1 and GJ2, gas targets; Al, aluminum filter; HM, hole-drilled mirror; TOF, time-of-flight detector. The Brewster window is typically oriented at ∼55° but can be varied to control the ratio of the gating field to the driving field.

A diagram of the optics is shown in Fig. 3(a). The input linearly polarized laser pulse is split into two orthogonal components by the first quartz plate at ±45° with respect to the input polarization. This plate also introduces a delay between the two pulses of a full number of optical cycles of the fundamental laser period. These two orthogonal components next pass through a fused silica window oriented at the Brewster angle and used to reject a portion of the field component lying along the input polarization while leaving the other field component unchanged. The fused silica window is as thin as possible—in our case 0.5 mm—in order to minimize dispersion. These modified pulses then pass through the second quartz plate and the BBO crystal together acting as a quarter-wave plate. The BBO is for second-harmonic generation of ∼800-nm lasers with its optical axis cut at 29.2° for type I phase matching. Since the pulses do not have equal-magnitude electric-field components along the slow and fast axes of the two birefringent plates, right and left elliptically polarized pulses are generated. The superposition of these gives the ellipticity-dependent pulse containing a short linearly polarized portion that is the gate width at the center of the pulse. Depending on the input pulse duration, the thickness of the first quartz plate should be chosen to satisfy Eq. (5) being equal to one optical cycle. This equation implies that for longer pulse durations, T_d must be chosen to be larger, meaning thicker first quartz plates must be used. This result can be varied slightly by changing ε and is accomplished experimentally by tuning the angle of the fused silica window.

The duration of the gate width determines how many attosecond pulses are generated. If the gate width is sufficiently narrow, only one pulse can be supported, effectively isolating a single attosecond pulse. Also, since the final plate is a BBO crystal, a weak linear second-harmonic field is generated which, due to the type-I phase-matching of the crystal, lies along the driving portion of the ellipticity-dependent pulse. The purpose of the second harmonic is to break the symmetry of the driving field, thereby allowing harmonic emission only once per optical cycle. This means the gate width can be a full optical cycle and still only allow one attosecond pulse. A measurement of the second-harmonic power after filtering the residual fundamental laser with four bounces on narrow-band reflecting dielectric mirrors allowed us to estimate the second-harmonic intensity at the interaction region. The result indicated that the second harmonic had field strength ∼15% of the fundamental laser pulse.

IV. ATTOSECOND PULSE GENERATION AND CHARACTERIZATION

The 25-fs pulses generated by the amplifier (see the Appendix) were used to generate an ellipticity-dependent pulse with the GDOG technique. To temporally characterize the attosecond pulses, an attosecond streak camera was used as shown in Fig. 3(b). A linearly polarized 25-fs laser pulse was split by a broadband 80:20 beam splitter with the majority of the beam being used for the attosecond pulse generation. This beam passed through the first quartz plate, the fused silica window, and the second quartz plate before being focused by an $f = 375$ mm spherical mirror. The focused beam passed through a fused silica entrance window to the vacuum chamber and then through the BBO crystal of the GDOG optics. The BBO was located inside the vacuum to avoid the group delays between the fundamental and second-harmonic beams when passing through the vacuum window. The beam was then focused onto an argon gas target to generate the attosecond pulse. The gas target was placed ∼2 mm after the laser focus to optimize the phase matching

of the attosecond pulse generation process. The attosecond pulse then passed through an aluminum filter to compensate the intrinsic chirp of the attosecond pulse and also to filter out the residual fundamental laser. Meanwhile, the reflected portion of the original laser pulse passed through a delay stage and recombined with the attosecond pulse at a hole-drilled mirror. The mirror allowed the attosecond pulse to pass and reflected the fundamental laser. This portion of the laser pulse remained linearly polarized for attosecond streaking.

In order to temporally stabilize the generation and streaking arms of the Mach-Zehnder interferometer-type setup, a continuous wave laser with 532-nm center wavelength was co-propagated with the fundamental laser. The beam that propagated with the XUV beam reflected off the backside of the hole mirror while the beam that propagated with the streaking beam passed through the hole. These two beams were then overlapped and an interference pattern was generated. A photodiode monitored the fringe pattern and the output signal was used as feedback control for a piezoelectric transducer (PZT) attached to a mirror in the interferometer. This allowed active control over the optical path lengths of both arms of the interferometer, giving accurate temporal stabilization. Using this method, the temporal jitter was measured to be ~8 as.

The two beams were then focused to a second gas target by a concentric set of Mo/Si and Ag spherical mirrors for the attosecond pulse and the fundamental pulse, respectively. The second target was krypton gas and was used to generate photoelectrons from the attosecond pulse, which were then given a momentum shift whose magnitude depended on the vector potential of the fundamental laser. Krypton was chosen due to its lower ionization potential. This shifts the photoelectrons up in energy so that they are easily distinguishable from the preceding threshold ionization peaks found at near zero energy. The attosecond pulse was then delayed with respect to the fundamental beam using a PZT attached to the Mo/Si mirror.

The photoelectrons next passed through a cone with a hole at the tip to isolate the gas nozzle from the detector. The photoelectrons then entered a region of uniform magnetic field generated by a set of Helmholtz coils and were incident onto a position-sensitive time-of-flight electron spectrometer with an energy resolution better than 0.6 eV at 35 eV [22]. The momentum spectrum and hence the energy of the photoelectrons was then collected as a function of the delay between the attosecond pulse and the streaking laser field, yielding a two-dimensional streaked spectrogram. Using the iterative principle components generalized projections algorithm (PCGPA) [23], the attosecond pulse and phase were reconstructed.

V. EXPERIMENTAL RESULTS AND DISCUSSION

A. Dependence of attosecond electron spectrum on CE phase

Previously it was shown that the generated attosecond XUV spectrum has a strong dependence on the CE phase of the driving laser [15,24]. Since the gating method chosen in this experiment has the contribution of the second harmonic which breaks the symmetry of the driving laser, we expect a full-cycle periodicity with GDOG, as was seen in DOG.

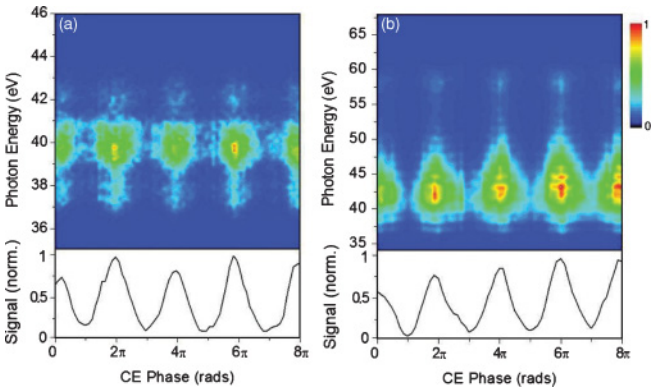

FIG. 4. (Color online) (a) The photoelectron energy spectrum plotted as a function of the CE phase of the input laser. The generation gas is argon. The plot at the bottom is the signal strength integrated along the energy axis. (b) The photoelectron spectrum from a generation gas target of neon plotted as a function of the CE phase. The plot at the bottom represents the signal integrated along the energy axis.

When the gate width is less than an optical cycle, the CE phase determines where the attosecond pulse is generated inside the polarization gate, thereby varying the attosecond-pulse-generation efficiency. The strongest attosecond pulse is produced for the CE phase value that generates the pulse at the center of the gate.

Figure 4(a) shows a CE phase scan of the photoelectron spectrum corresponding to the attosecond pulses generated from argon gas. The scans were taken with the attosecond streak camera's photoelectron detector, thereby mimicking the actual experimental conditions when the pulse duration was measured. The 2π periodic structure is obvious, indicating the two-color gating effect. Each slice was integrated for 30 s while the CE phase was slowly swept from 0 to 2π. The spectrum is fairly continuous, covering a broad range of the CE phase. The implication is that our gate width is actually less than one optical cycle. The width of the integrated attosecond-signal curve [bottom plot of 4(a)] in the 2π CE phase range is a measure of the gate width. The signal nearly reaches zero for certain values of the CE phase, implying that the gate width is less than one cycle. At those values of CE phase, there is no pulse within the linear portion to contribute to the attosecond pulse strength.

Figure 4(b) is a similar result to Fig. 4(a) but with neon as the target gas. Here, the integration time is 60 s per slice. The high-energy portion is strongly modulated along the CE phase axis, indicating a strong dependence of the ellipticity on the XUV photon generation process. The lower-energy portion shows a weaker dependence, however. Also in this case, the spectra are fairly continuous over all values of the CE phase, which is similar to previous results [15,24], which indicates that isolated attosecond pulses are always generated even if the CE phase is not stabilized for such a narrow gate width. Conversely, locking the CE phase to the value of the highest photoelectron yield will maximize the count rate, which is always crucial for photoelectron experiments. Also, the total signal integrated along the energy axis is shown in the bottom plot of Fig. 4(b). This shows similar modulation depth to the

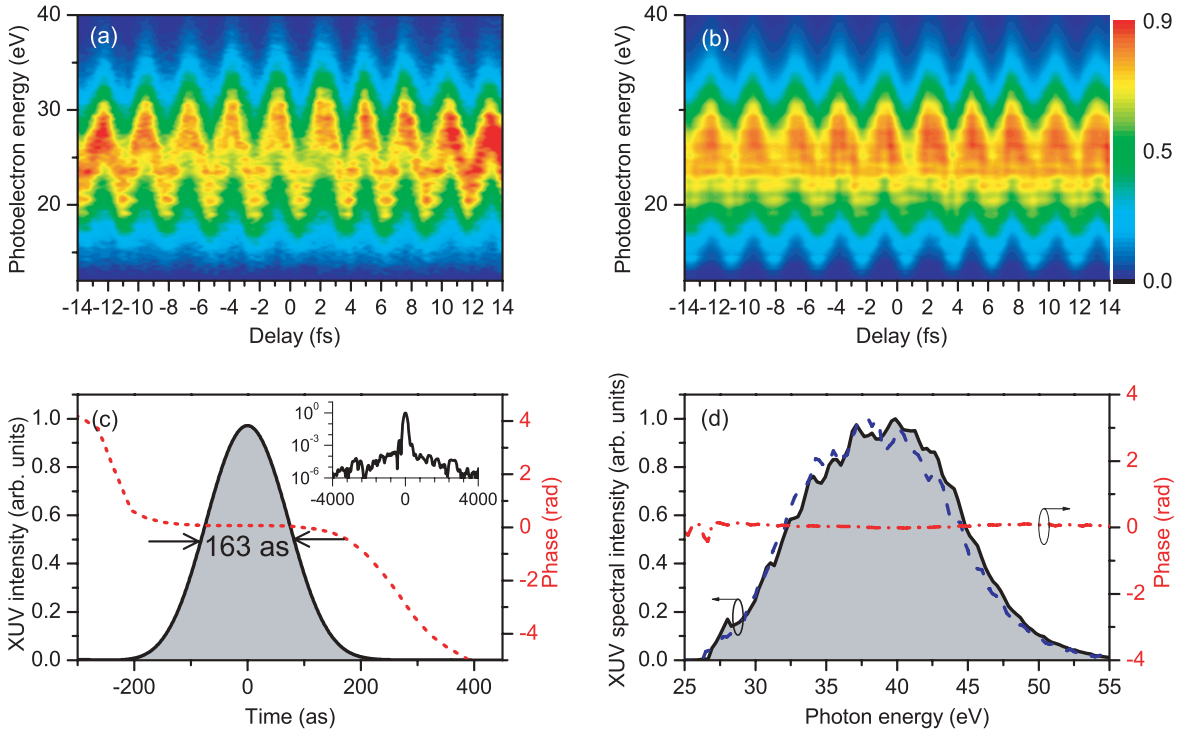

FIG. 5. (Color online) The experimentally obtained (a) and retrieved (b) streaked spectrograms of a multicycle laser pulse. The temporal profile (solid line) and temporal phase (dotted line) are shown in Fig. (3). The inset figure shows the same temporal profile but over an extended temporal range. The pre- and postpulses located at ±2600 as are less than 0.1% of the main pulse. Panel (d) shows the experimental (dashed line) and retrieved (solid line) XUV-only spectrum. The dashed-dotted line shows the spectral phase and indicates in this case that the pulse is nearly transform limited.

integrated signal in Fig. 4(a), indicating agreement with the narrow gate width estimate.

These results demonstrate CE phase effects on the longest pulse durations yet (∼25 fs). Since the gating method also covers the lowest harmonic orders, it is conceivable that this method can be extended to gate above-threshold ionization electron spectra even for pulses as long as 25 fs. This allows CE phase meters to be constructed for use with pulses directly from an amplifier [25].

B. Temporal characterization

Figure 5 shows the results of the temporal characterization of the attosecond pulse with 60-s integration per delay slice. Figures 5(a) and 5(b) show the experimental and reconstructed streaked spectrograms, respectively. The figures contain 10 cycles as this increases the accuracy of the reconstruction due to the redundant data. Figure 5(c) shows the temporal profile of the pulse (solid line) and the temporal phase (dotted line). The flat phase indicates a nearly transform-limited pulse and the full width at half maximum (FWHM) of the pulse indicates 163 as duration. The transform-limited pulse duration of this result is calculated as ∼163 as. The inset figure shows the temporal profile over a several-cycle range. This indicates that the contributions from pre- and postpulses are less than 0.1% of the main peak demonstrating that the pulse is indeed an isolated attosecond pulse. Figure 5(d) shows a comparison between the experimental XUV-only spectrum (dashed line) and the retrieved XUV spectrum (solid line) from the retrieved temporal profile and phase shown in Fig. 5(c). The accuracy of this result indicates that we can trust our reconstruction. Also shown is the retrieved spectral phase (dashed-dotted line). This shows the pulse to be nearly transform-limited.

C. Effect of statistical noise

For the same laser energy, GDOG for 25-fs pulses produces fewer photons than DOG for 8-fs pulses due to the increased depletion of the ground state. This results in the necessity for longer integration times as compared with short-pulse DOG. It has previously been found in the case of DOG, however [26], that the peak count of the XUV spectra generated is the deciding factor in whether the attosecond pulse can be reconstructed or not. To find the lower limit of the peak count number and hence the integration time necessary to accurately reconstruct an attosecond pulse, we compared reconstructions of traces with varying integration times. Since our data acquisition software saves the full photoelectron spectrum for each laser shot, we can simply extract the data accumulated in differing time windows. These new data sets were then individually reconstructed and the retrieved pulse duration, temporal profile, and phase were compared.

Figure 6(a) shows a comparison of the temporal profile for the same attosecond pulse but with accumulation times of 60 s (red solid line) and 1 s (blue solid line). Also shown are the corresponding temporal phases for the 60-s (red dashed line) and 1-s (blue dashed line) cases. The FWHM of both pulses are nearly identical and the temporal phases have

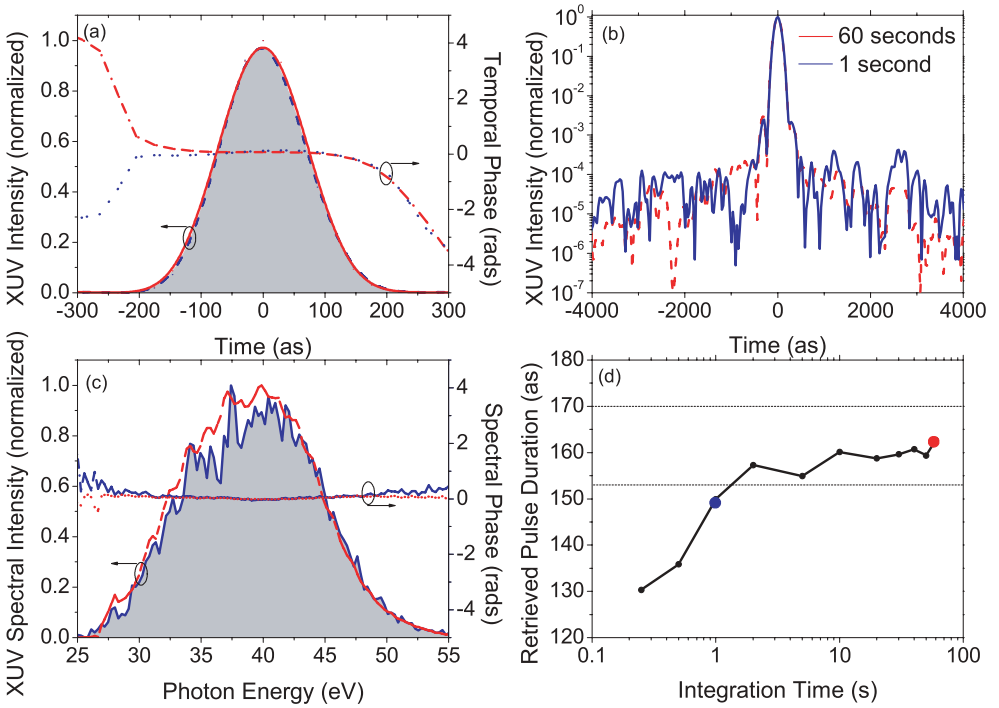

FIG. 6. (Color online) (a) The temporal profiles for 60s and 1s integration times (red dashed and blue solid lines, respectively). The red dot-dash and blue dotted lines indicate the 60-s and 1-s temporal phases, respectively. (b) The temporal profiles for 60 s (red dashed line) and 1 s (blue solid line) shown over an extended time range to demonstrate the small contributions from the pre- and postpulses. (c) The retrieved XUV spectra (red dashed and blue solid lines) and spectral phase (red dotted and blue dot-dashed lines) for 60-s and 1-s integration times, respectively. (d) The retrieved pulse duration plotted as a function of the integration time. The red (upper) circle represents the 60-s integration time result and the blue (lower) circle represents the 1-s integration time result. The horizontal dashed lines indicate a $\pm 5\%$ pulse duration range centered at 163 fs.

identical shapes. An extended view of the temporal profile is shown in Fig. 6(b). Here the time range extends beyond one optical cycle, indicating almost no contribution from pre- and postpulses. The 1-s integration (blue line) has a higher noise level than the 60 s (red line) integration time due to the increased statistical noise in the 1-s integration time.

To compare the reconstructions, Fig. 6(c) shows the reconstructed XUV power spectra for the 60-s (red solid line) and 1-s (blue solid line) cases. The agreement is close, with the 1-s case being slightly more modulated due to the reduced signal-to-noise ratio. Also shown are the spectral phases for the 60-s and 1-s cases (red and blue dashed lines, respectively).

Finally, Fig. 6(d) shows the retrieved pulse duration plotted as a function of integration time of the energy spectrum. The horizontal dashed lines on the plot show a window of $\pm 5\%$ of the 60-s pulse duration result (163 as). The points from 60 to 1 s lie within this range and are considered to be accurate reconstructions. The blue (lower) circle represents the 1-s integration time and the red (upper) circle represents the 60-s integration time. The peak count of the 1-s integration time was $\sim$50, which agrees with the results of other work [26]. This implies that the peak counts of the spectrum should be at least 50 to accurately reconstruct the pulse.

For our experimental conditions, 50 counts required 1 s of integration time. This amount of photon flux corresponded to pulse energies of $\sim$170 pJ before the aluminum filter. To estimate the attosecond pulse energy, we generated an identical attosecond pulse in a photon spectrometer [13] that had an XUV photodiode installed after the Al filter. This allowed us to measure the pulse energy and the spectrum that was being generated in the attosecond streak camera. The measured result was corrected from losses associated with transmission through the Al filter ($\sim$300 μm thick). The photoelectron spectrum was then scaled by the results from the photon spectrometer. The attosecond pulse energy is limited by the input laser power. In our case, we only have 2 mJ at our disposal. However, if the GDOG method was used on pettawatt-class lasers or lasers capable of delivering several joules of pulse energy, the corresponding attosecond pulse energy could be scaled to previously unattainable levels.

VI. CONCLUSIONS

We optimized a multipass amplifier to generate 25-fs, 2-mJ laser pulses. These pulses were then used to generate single isolated attosecond pulses with the GDOG technique. A CE phase scan of the attosecond pulses showed a 2π periodicity, which demonstrates the robustness of our GDOG gating scheme. The attosecond pulse energy was measured to be $\sim$170 pJ, which was comparable to other gating schemes relying on much shorter input pulse durations [24].

Temporal characterization of the attosecond pulses showed $\sim$163 as pulses were generated. The role of statistical noise in the spectra was also shown to be negligible even for integration times of $\sim$1 s, corresponding to peak spectral counts of $\sim$50 in agreement with previous results from DOG. This allows a

full streaked spectrogram capable of accurately reconstructing attosecond pulses from 25-fs lasers to be acquired in a few minutes, thereby significantly improving the ability of the streak camera to be a daily characterizer of attosecond pulses generated in the laboratory. Using the GDOG technique will allow many labs to generate single attosecond pulses of XUV photons directly from an amplifier, which should help further expand the field of attosecond science.

ACKNOWLEDGMENTS

This material is by the US Army Research Office under Grant No. W911NF-07–1-0475, and by the US Department of Energy.

APPENDIX: CHIRPED PULSE AMPLIFIER FOR GDOG

Although the GDOG works with pulses as long as 28 fs, it is still beneficial to reduce the amplifier pulse duration. This is because the laser-to-attosecond-pulse conversion efficiency is higher for shorter laser pulse durations. We implemented a simple scheme to shorten the laser pulse. The full laser setup is shown in Fig. 7 with panel (a) showing the Kansas Light Source (KLS) laser system [27]. The front end of the KLS system consists of a Kerr-lens mode-locked Ti:sapphire oscillator (FemtoSource Pro), with 1.5-kHz pulses with ~100 nm bandwidth and 3 nJ energy picked by a Pockels cell from the oscillator pulse train. These were then stretched to ~80 ps by a grating-based Martinez type stretcher. The CE phase of the oscillator was locked by the self-referencing technique [28,29] and the slow drift in the amplifier was compensated through feedback control of the grating separation in the stretcher [30–32]. Then, the stretched pulses were amplified to 5 mJ with a Ti:sapphire 14-pass amplifier, with the Ti:sapphire crystal cooled to liquid nitrogen temperature to reduce the thermal lens effect. After the first 7 passes, the preamplified pulses were extracted from the amplifier and passed through a telescope to match the pump laser size so that the pump energy could be efficiently extracted for the second-stage 7 passes. Another Pockels cell which generates a 10-ns window was used to suppress the amplified spontaneous emission generated during the preamplification process. After the amplification, the pulses were compressed by a pair of gratings to 2 mJ, 33 fs, with 26 nm FWHM spectrum bandwidth. We intentionally mismatched the gratings in the stretcher (1200 grooves/mm) to the gratings in the compressor (1400 grooves/mm) to suppress the fourth-order phase distortion [33].

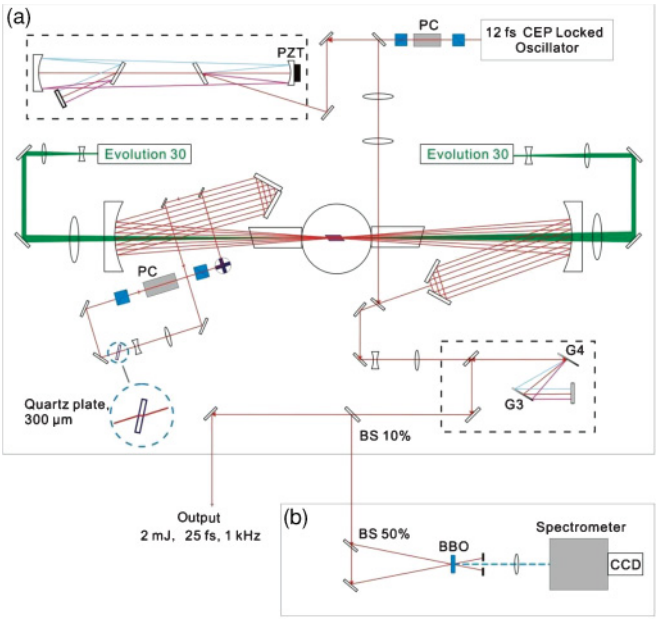

FIG. 7. (Color online) (a) Schematic of the laser system. Two diode-pumped Q-switched Nd:YLF Evolution 30 lasers were used to pump the gain medium. G1, G2 1200 g/mm gratings, G3, G4 1400 g/mm, mismatching gratings concept was applied to reduce high-order phase distortion. PC is a pockels cell. (b) Schematic of the SHG-FROG. The solid line represents the fundamental beam and the dashed line represents the second-harmonic beam. BBO is a type-I phase-matching crystal with 5-μm thickness. BS is a beam splitter.

The width of the stimulated emission cross section curve of the Ti:sapphire crystal in the liquid nitrogen temperature is narrower than that in the room temperature. The 33-fs duration is set by the gain narrowing in the amplifier when the crystal is cooled. In order to generate a spectrum capable of supporting 25 fs for the GDOG experiment, a 300-μm-thick birefringent quartz plate (BP) was inserted as a spectrum shaping filter before the polarizer between the first and second 7 passes. It introduced higher loss at the central frequency than that of the wings of the gain, thus compensating the effects of the gain narrowing [34]. A formula for calculating the birefringent quartz plate's single-pass transmission provided in Ref. [35] was combined with the gain calculation method in Ref. [36] for simulating our amplifier. The calculated amplified output spectrum reached 50 nm FWHM, as shown in Fig. 8(a) (solid line). This agreed well with the experimentally optimized result (dashed line). Figure 8(b) shows the measured 7-pass spectrum before (solid curve) and after the plate and a polarizer (dashed).

We characterized the final output pulses by using a single-shot, second-harmonic generation frequency-resolved optical gating (SHG-FROG). The FROG setup is shown in Fig. 7(b). Ten percent of the output beam from the amplifier was diverted to the SHG-FROG, where it was split evenly into two parts with a broadband beam splitter. The reflected

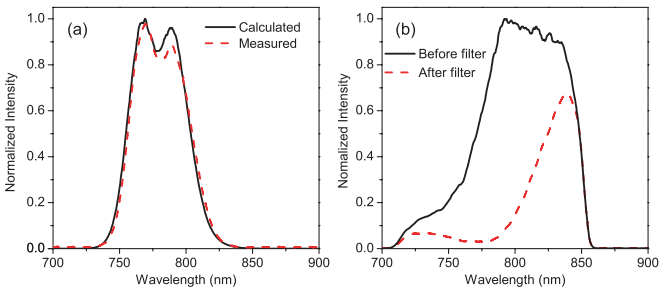

FIG. 8. (Color online) Calculated and experimental spectrum for the birefringent plate spectrum shaping. (a) Calculated (solid) and measured (dashed) amplified output spectrum with BP. (b) Measured 7-pass spectrum before the plate (solid curve) and after the plate and a polarizer (dashed).

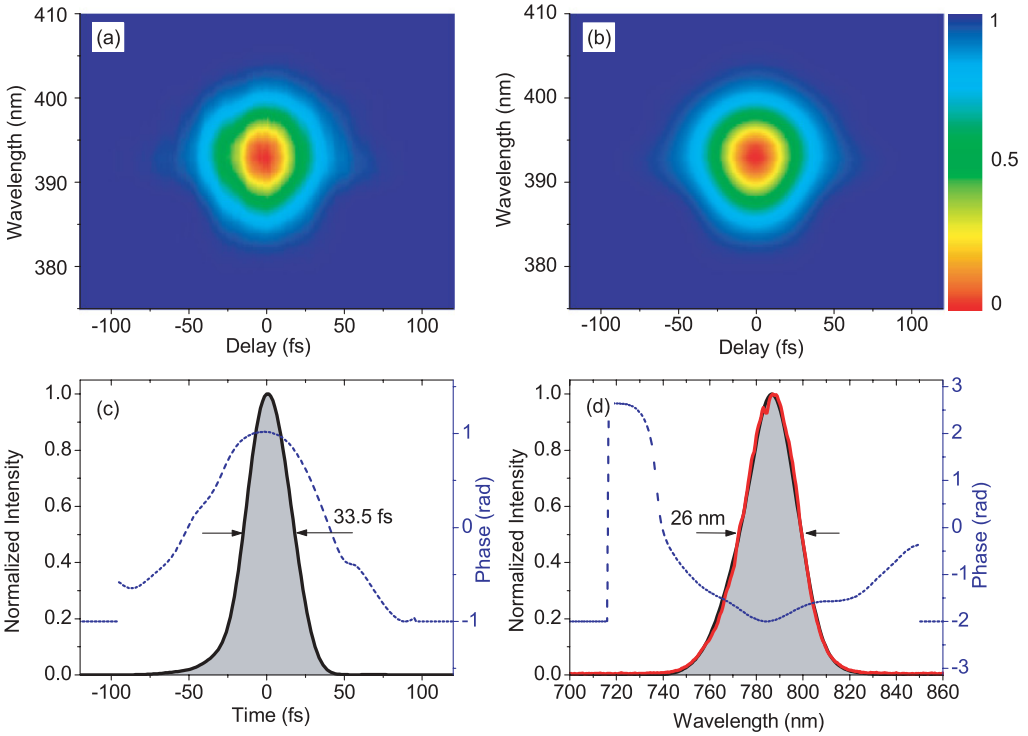

FIG. 9. (Color online) Characterization of the 33-fs laser pulse by the FROG. (a) The measured FROG trace. (b) The reconstructed FROG trace. (c) The retrieved pulse shape (solid line) and phase (dashed line). (d) The retrieved power spectrum (solid black line) and phase (dashed line) and independently measured spectrum (solid red line).

beam, after passing through a compensating plate, and the transmitted beam cross with a small angle at a 5-μm-thick, type-I BBO crystal (phase-matching angle of 29.2°) with a 1 cm^2 aperture for the second-harmonic generation. The second-harmonic signal was then spatially filtered out from the fundamental beam and diverted to a spectrograph with

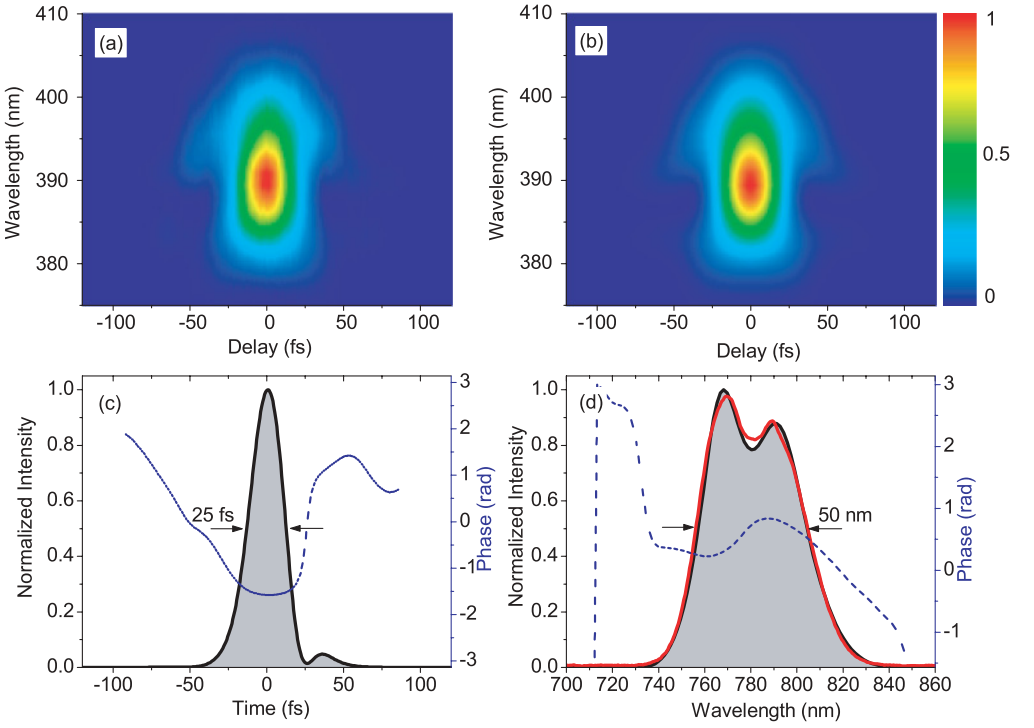

FIG. 10. (Color online) Characterization of the 25-fs laser pulse by the FROG. (a) The measured FROG trace. (b) The reconstructed FROG trace. (c) The retrieved pulse shape (solid line) and phase (dashed line). (d) The retrieved power spectrum (solid black line) and phase (dashed line) and independently measured spectrum (solid red line).

a UV CCD camera as a detector. The crystal was imaged onto the entrance slit of the spectrometer with a lens of focal length 250 mm and demagnification of $\frac{1}{2}$. A time delay between the two pulses along the slit is introduced due to the noncollinear geometry of the two beams on the BBO. Finally, a commercially available FROG algorithm (Femtosoft FROG) was used to reconstruct the original pulse from the measured FROG trace. The FWHM of the measured pulse was 33 fs without the quartz plate spectrum filter. The measured and reconstructed FROG patterns are shown in Figs. 9(a) and 9(b), respectively. The retrieved 33-fs pulse is shown in Fig. 9(c). Figure 9(d) shows the retrieved spectrum together with an independently measured spectrum. The 25-fs pulse FROG trace was measured with the same setup after the quartz spectrum filter was installed. Figure 10(a) is the measured trace and Fig. 10(b) the retrieved trace. Figure 10(c) shows the retrieved pulse shape in the time domain with the phase. The output spectrum from the amplifier was broadened to 50 nm in both the retrieved and the independently measured spectrum, as shown in Fig. 10(d).

[1] A. Scrinzi, M. Yu Ivanov, R. Kienberger, and D. M. Villeneuve, J. Phys. B **39**, R1 (2006).

[2] E. Gouielmakis, V. Yakovlev, A. L. Cavaleri, M. Uiberacker, V. Pervak, A. Apolonski, R. Kienberger, U. Kleineberg, and F. Krausz, Science **317**, 769 (2007).

[3] M. F. Kling *et al.*, *2008 Conference on Lasers and Electro-Optics (CLEO)*, paper J1H1.

[4] A. L. Cavalieri *et al.*, Nature (London) **449**, 1029 (2007).

[5] A. Baltuska, Th. Udem, M. Uiberacker, M. Hentschel, E. Goulielmakis, Ch. Gohle, R. Holzwarth, V. S. Yakolev, A. Scrinzi, T. W. Hansch, and F. Krausz, Nature (London) **421**, 611 (2003).

[6] P. B. Corkum, N. H. Burnett, and M. Y. Ivanov, Opt. Lett. **19**, 1870 (1994).

[7] V. T. Platonenko and V. V. Strelkov, J. Opt. Soc. Am. B **16**, 435 (1999).

[8] O. Tcherbakoff, E. Mével, D. Descamps, J. Plumridge, and E. Constant, Phys. Rev. A **68**, 043804 (2003).

[9] Z. Chang, Phys. Rev. A **70**, 043802 (2004).

[10] G. Sansone, E. Benedetti, F. Calegari, C. Vozzi, L. Avaldi, R. Flammini, L. Poletto, P. Villoresi, C. Altucci, R. Velotta, S. Stagira, S. De Silvestri, and M. Nisoli, Science **314**, 443 (2006).

[11] E. Goulielmakis, M. Schultz, M. Hofstetter, V. S. Yakolev, J. Gagnon, M. Uiberaker, A. L. Aquila, E. M. Gullikson, D. T. Attwood, R. Kienberger, F. Krausz, and U. Kleineberg, Science **320**, 1614 (2008).

[12] H. Mashiko, S. Gilbertson, C. Li, S. D. Khan, M. M. Shakya, E. Moon, and Z. Chang, Phys. Rev. Lett. **100**, 103906 (2008).

[13] S. Gilbertson, H. Mashiko, C. Li, S. D. Khan, M. M. Shakya, E. Moon, and Z. Chang, Appl. Phys. Lett. **92**, 071109 (2008).

[14] Y. Oishi, M. Kaku, A. Suda, F. Kannari, and K. Midorikawa, Opt. Express **14**, 7230 (2006).

[15] S. Gilbertson, H. Mashiko, C. Li, E. Moon, and Z. Chang, Appl. Phys. Lett. **93**, 111105 (2008).

[16] V. Yanovsky, V. Chvykov, G. Kalinchenko, P. Rousseau, T. Planchon, T. Matsuoka, A. Maksimchuk, J. Nees, G. Cheriaux, G. Mourou, and K. Krushelnick, Opt. Express **16**, 2109 (2008).

[17] Z. Chang, Phys. Rev. A **76**, 051403(R) (2007).

[18] X. Feng, S. Gilbertson, H. Mashiko, H. Wang, S. Khan, M. Chini, Y. Wu, K. Zhao, and Z. Chang, Phys. Rev. Lett. **103**, 183901 (2009).

[19] Y. Mairesse and F. Quere, Phys. Rev. A **71**, 011401(R) (2005).

[20] M. V. Ammosov, N. B. Delone, and V. P. Krainov, Sov. Phys. JETP **64**, 1191 (1986).

[21] P. B. Corkum, Phys. Rev. Lett. **71**, 1994 (1993).

[22] X. Feng, S. Gilbertson, S. Khan, M. Chini, Y. Wu, K. Carnes, and Z. Chang, Opt. Express **18**, 1316 (2010).

[23] M. Chini, H. Wang, S. D. Khan, S. Chen, Z. Chang, Appl. Phys. Lett. **94**, 161112 (2009).

[24] I. J. Sola, E. Mével, L. Elouga, E. Constant, V. Strelkov, L. Poletto, P. Villoresi, E. Benedetti, J.-P. Caumes, S. Stagira, C. Vozzi, G. Sansone, and M. Nisoli, Nat. Phys. **2**, 319 (2006).

[25] G. G. Paulus, F. Lindner, H. Walther, A. Baltuska, E. Goulielmakis, M. Lezius, and F. Krausz, Phys. Rev. Lett. **91**, 253004 (2003).

[26] H. Wang, M. Chini, S. D. Khan, S. Chen, S. Gilbertson, X. Feng, H. Mashiko, and Z. Chang, J. Phys. B **42**, 134007 (2009).

[27] B. Shan, C. Wang, and Z. Chang, U.S. Patent No. 7050474, issued May 23, 2006.

[28] D. J. Jones, S. A. Diddams, J. K. Ranka, A. Stentz, R. S. Windeler, J. L. Hall, and S. T. Cundiff, Science **288**, 635 (2000).

[29] E. Moon, C. Li, Z. Duan, J. Tackett, K. L. Corwin, B. R. Washburn, and Z. Chang, Opt. Express **14**, 9758 (2006).

[30] C. Li, E. Moon, and Z. Chang, Opt. Lett. **31**, 3113 (2006).

[31] Z. Chang, Appl. Opt. **45**, 8350 (2006).

[32] C. Li, E. Moon, H. Mashiko, C. M. Nakamura, P. Ranitovic, C. M. Maharjan, C. L. Cocke, Z. Chang, and G. G. Paulus, Opt. Express **14**, 11468 (2006).

[33] J. D. Bonlie, F. Patterson, D. Price, B. White, and P. Springer, Appl. Phys. B **70**, S155 (2000).

[34] C. P. J. Barty, G. Korn, F. Raksi, C. Rose-Petruck, J. Squier, A.-C. Tien, K. R. Wilson, V. V. Yakovlev, and K. Yamakawa, Opt. Lett. **21**, 219 (1996).

[35] X. Lu, C. Li, Y. Leng, C. Wang, C. Zhang, X. Liang, R. Li, and Z. Xu, Chin. Opt. Lett. **5**, 493 (2007).

[36] Z. Cheng, F. Krausz, and Ch. Spielmann, Opt. Commun. **201**, 145 (2002).